agriculture

MDPI

Article

Parameter Optimization of Spiral Step Cleaning Device for Ratooning Rice Based on Computational Fluid Dynamics-Discrete Element Method Coupling

Weijian Liu [1], Shan Zeng [2] and Zhandong Wu [1,*]

[1] Faculty of Modern Agricultural Engineering, Kunming University of Science and Technology, Kunming 650500, China; 1000005920@ujs.edu.cn
[2] College of Engineering, South China Agricultural University, Guangzhou 510642, China; shanzeng@scau.edu.cn
* Correspondence: zhdwu1989@gmail.com

Abstract: Ratooning rice plants have a high moisture content and strong adhesion during harvesting. Traditional cleaning devices are prone to clogging when processing ratooning rice, resulting in a series of problems such as high grain loss rate and high grain impurity rate. In response to the above issues, this article adopts the CFD-DEM coupling method to design a spiral step cleaning device. A detailed analysis was conducted on the influence of the cone angle and thickness of the spiral-stepped skeletons on the flow state, and flow velocity and pressure distribution cloud maps were obtained under different structural parameters. The vortex morphology under different thicknesses of the spiral-stepped skeletons was compared, and the structural parameters of the device were determined. The motion trajectory and distribution of impurity particles under different inlet flow velocities were analyzed using data superposition, and the appropriate inlet flow velocity range was determined. A test bench was built, and a three-factor quadratic regression orthogonal rotation combination experiment was conducted with fan speed, feeding rate, and device inclination angle as experimental factors. The results of the bench test show that the performance index reaches its optimum when the device inclination angle, fan speed, and feeding rate are 2.47°, 2906 r/min, and 4.0 kg/s, respectively. At this time, the grain impurity rate, grain loss rate, and sieve clogging rate are 2.21%, 2.15%, and 3.5%, respectively. Compared to those of traditional cleaning equipment, these value are reduced by 44.5%, 39.6%, and 83.9%, respectively. This study can provide ideas for the design of ratooning rice cleaning devices.

Keywords: ratooning rice; spiral step cleaning; data superposition; CFD-DEM; test

Citation: Liu, W.; Zeng, S.; Wu, Z. Parameter Optimization of Spiral Step Cleaning Device for Ratooning Rice Based on Computational Fluid Dynamics-Discrete Element Method Coupling. *Agriculture* **2024**, *14*, 2141. https://doi.org/10.3390/agriculture14122141

Academic Editor: Mustafa Ucgul

Received: 29 October 2024
Revised: 21 November 2024
Accepted: 23 November 2024
Published: 25 November 2024

1. Introduction

The rice growing area in China is about 30 million hectares, with an annual output of more than 210 million tons [1–3]. According to the statistics of the Ministry of Agriculture of the People's Republic of China in 2020, there are 2328 rice varieties, five rice planting areas, and three rice planting methods in China. Among them, ratooning rice has been rapidly promoted in suitable planting areas in the middle and lower reaches of the Yangtze River in recent years due to its advantages of two harvests, increased grain yield and income, and good rice quality [4–7]. Due to the high moisture content and strong adhesion of ratooning rice during harvesting, it is very common for the sieve to become clogged during cleaning. If the sieve becomes clogged during operation, it will reduce the effective screening area of the sieve surface, causing the ratooning rice to be unable to pass through. On the other hand, a blockage on the surface of the sieve reduces the airflow velocity and uniformity, resulting in a sharp increase in grain impurity and loss rates, which seriously affects the stability of the harvester. Therefore, sieve blockage is an urgent problem to be explored and solved in the cleaning of ratooning rice.

In recent years, the coupling of CFD-DEM gas–solid two-phase flow has been widely used in the agricultural field [8–11]. In order to achieve the efficient cleaning of ratooning rice grains, this paper presents a spiral step cleaning device based on the characteristics of the cleaning device of the ratooning rice harvester. The problem of sieve blockage is solved by the rotation and revolution of the vortex in the groove. CFD-DEM gas–solid coupling is used for the numerical analysis of the cleaning device, and a spiral step blockage elimination mechanism is established to fully utilize the advantages of spiral step high-efficiency cleaning, reduce the blockage rate, and improve the comprehensive cleaning performance of the cleaning device.

2. Structure and Working Principle of Spiral Step Cleaning Device

2.1. Overall Design

The spiral step cleaning device is a biomimetic cleaning device designed based on the oral structure of filter-feeding fish such as sturgeon and basking sharks [12]. The main working component of the spiral step cleaning device designed in this article is the cleaning separation core, as shown in Figure 1a. The cleaning separation core consists of two spiral-stepped skeletons and a surface-covering screen mesh. The inlet diameter of the cleaning separation core is much larger than the outlet diameter. The clean ratooning rice grains are mainly discharged from the pores of the sieve, and the remaining impurities are discharged through the outlet of the cleaning separation core. In order to facilitate the description of the movement and the distribution of particles in the device, the cleaning groove and sieve area are named, as shown in Figure 1b,c. The sieves between adjacent skeletons are named the front sieve (Area I), middle sieve (Area II), and rear sieve (Area III).

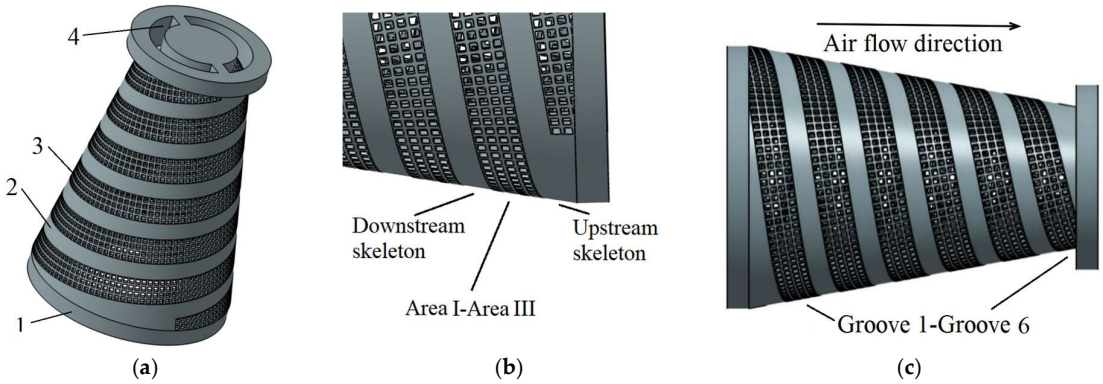

Figure 1. Structure diagram of cleaning separation core. 1. Mixture inlet 2. Spiral-stepped skeleton 3. Sieve 4. Impurity particle outlet. (**a**) Overall structure. (**b**) Adjacent spiral skeleton. (**c**) Distribution of grooves on the cleaning separation core.

2.2. Design of Airflow Device

The suspension velocity of agricultural materials is the basis for the design of pneumatic conveying systems and an important basis for setting reasonable conveying gas velocities [13–15]. Through preliminary experiments, the suspension velocity ranges of ratooning rice grains and impurity particles (straw) are 7.8–13.1 m/s and 4.2–6.8 m/s, respectively. There is no overlapping interval between the suspension velocities of ratooning rice particles and impurities, so this article only analyzes the aerodynamic characteristics of ratooning rice particles. When the ratooning rice grains are in a gas flow field, they are subjected to the gas force R and floating weight ω [16]:

$$\omega = \frac{\pi}{6} d_s^3 (\rho_s - \rho) g \tag{1}$$

$$R = C_d \frac{\pi}{4} d_s^2 \rho \frac{v_0^2}{2} \tag{2}$$

If the floating weight is greater than the gas force, the ratooning rice grains have a downward trend. When the floating weight is less than the gas force, the ratooning rice grains have an upward trend.

According to the mechanical formula for the floating weight and air resistance of ratooning rice grains in a suspended state, the following is derived:

$$C\frac{\pi}{4}d_s^2\rho\frac{v_0^2}{2} = \frac{\pi}{6}d_s^3(\rho_s - \rho)g \tag{3}$$

The formula for the suspension velocity of ratooning rice grains can be obtained as follows:

$$v_0 = \sqrt{\frac{4g}{3}\frac{d_s(\rho_s - \rho)}{C\rho}} \tag{4}$$

where v_0 is the suspension velocity of ratooning rice grains, m/s; d_s is the equivalent diameter of ratooning rice grains, m; ρ_s is the grain density of ratooning rice, kg/m^3; ρ is the air density, kg/m^3; C_d is the drag coefficient; C is the drag coefficient; and g is the gravitational acceleration, 9.81 m/s^2.

After entering the cleaning device, the grains collide with the wall under the action of the airflow, with a short collision time and small force, and the deformation of the grains can be ignored. The ratooning rice grains are subjected to forces in the airflow field, including gravity and buoyancy, contact force between grains, and forces between grains and airflow [17]:

$$m_p\frac{dv_p}{dt} = F_D + F_{GB} + F_{Sa} + F_{Ma} + F_C \tag{5}$$

where m_p is the mass of ratooning rice grains, kg; F_D is the fluid resistance, N; F_{GB} is the resultant force due to gravity and buoyancy, N; F_C is the collision contact force between the grain and the wall, N; v_p is the grain velocity, m/s; and F_{Sa} is the Saffman lift force, N.

The contact force between the ratooning grains and wall surface can be expressed as follows [18]:

$$F_C = F_n^d + F_t^d \tag{6}$$

where $F_t{}^d$ is the tangential damping force, N, and $F_n{}^d$ is the damping force between ratooning rice grain and wall, N.

Finally, the following formula is obtained [19]:

$$F_n^d = -2\sqrt{\frac{5}{6}}\frac{\ln e}{\sqrt{\ln^2 e + \pi^2}}\sqrt{S_n m^*}v_n \tag{7}$$

$$F_t^d = -2\sqrt{\frac{5}{6}}\frac{\ln e}{\sqrt{\ln^2 e + \pi^2}}\sqrt{S_t m^*}v_t \tag{8}$$

where m^* is the equivalent mass; S_n is the normal stiffness; e is the collision recovery coefficient; S_t is the tangential stiffness; v_t is the tangential component of the relative velocity at the contact point; and v_n is the normal component of the relative velocity at the contact point.

2.3. Step Cleaning Principle

When the mixture enters the cleaning separation core from the inlet, the cross-sectional area of the cleaning separation core gradually decreases along the axial direction, allowing the mixture to enter each cleaning groove. Due to the special structure of the spiral-stepped skeleton, the airflow in the cleaning groove will form a vortex, which can drive the mixture to rotate. The rotating mixture collides with the surface of the sieve mesh. Ratooning rice grains with a size smaller than the aperture of the sieve mesh can pass through the sieve, while larger impurities remain inside the device and continue to rotate with the vortex until they are discharged from the outlet of the device. Ratooning rice grains are mainly

discharged through rotation, while impurities are discharged through revolution. The mixture inside the device is cleaned under the dual action of rotation and revolution.

3. Numerical Calculation Method

3.1. Establishment of Particle Model

The moisture content of ratooning rice grains is 16~30%, the density is 983~1369 kg/m^3, and the shape is approximately ellipsoidal [20,21]. The geometric dimensions are 9.00 mm × 1.91 mm × 4.0 mm (length × width × height). The main component of impurities is broken straw, and the fracture mode is mainly axial fracture, with almost no radial fracture. The length is about 20–40 mm, and the radius is about 5–7 mm. In order to study the separation process of ratooning rice grains and straw, a model of ratooning rice grains and straw was established by stacking multiple spheres. In order to improve computational efficiency and reduce computational complexity, the model did not consider leaves and assumed that the cross-sectional area and structure of straw were uniform. Virtual experiments were used to calibrate the simulation parameters of the ratooning rice grains and impurities, and the indirect contact property parameters of the two materials were obtained, as shown in Tables 1 and 2. The cleaning separation core skeleton and screen mesh are both made of nylon material.

Table 1. Simulation parameter settings.

Item	Poisson's Ratio	Shear Modulus/(Mpa)	Density/(kg·m^{-3})
Ratooning rice	0.30	26	1300
Short straw	0.40	10	100
Nylon (clear separation core)	0.28	0.027	1072

Table 2. Contact coefficients in EDEM.

Item	Restitution Coefficient	Static Friction Coefficient	Rolling Friction Coefficient
Grain–grain	0.2	1.0	0.03
Grain–short straw	0.2	0.8	0.02
Grain–nylon	0.5	0.58	0.04
Short straw–short straw	0.2	0.90	0.01
Short straw–nylon	0.2	0.7	0.03

3.2. Model Establishment and Boundary Conditions

The main structural parameters that affect the formation of vortices in the groove include the thickness of the spiral-stepped skeleton h [22], the ratio of the inlet area to the screen area F [23], the cone angle γ, and the groove angle α, as shown in Figure 2. The basic condition for the formation of vortices in the groove during the step cleaning process is that the ratio G of the groove width w to the thickness of the spiral-stepped skeleton h is less than 3 [21,24]. Considering the quality of the cleaning separation core, the thickness of the spiral-stepped skeleton is set to 20 mm~60 mm, and the proportional coefficient G is taken as 2, resulting in a groove height of 40 mm~120 mm. If the cone angle value is too large, the outlet diameter will be very small, affecting the discharge rate of impurities. If the cone angle value is too small, the difference between the inlet diameter and the outlet diameter will be small, making it difficult for the mixture to enter the cleaning groove and affecting the cleaning effect. After single-factor testing, the range of cone angle values was determined to be 6.5°~14.5°. The ratio F between the inlet area and the screen area is a key parameter for the formation of vortices in the cleaning groove, and usually, its value should be greater than 1 [25]. The remaining structural parameters are set as follows: groove angle α = 105°, inlet area S_{in} = 2.8 × 10^5 mm^2, screen area S_m = 1.02 × 10^6 mm^2, and screen aperture O = 15 mm.

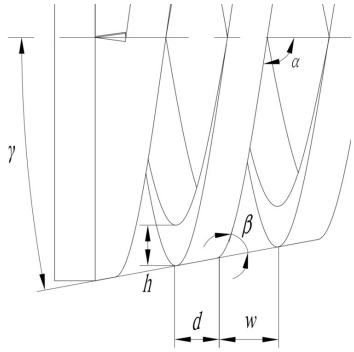

Figure 2. Main parameters of cleaning separation core.

Grid division is crucial for the numerical simulation results. The model adopts a hexahedral structured grid. In order to ensure the accuracy of the calculation, the grid is densified at the junction of the sieve mesh to improve accuracy, and grid independence is tested by increasing the number of model nodes by 1.5, 2, and 3 times, respectively. The numerical simulation results are all within the allowable convergence error range. Therefore, the final selection of the number of grid nodes in the computational domain is 9.6×10^5. Due to the presence of reflux and jet phenomena inside the cleaning separation core [26], the standard k-ε model is adopted [27]. The inlet is set as a velocity inlet condition, with the same inlet velocity for both gas and particle phases. The outlet is set as a pressure outlet condition, with standard atmospheric pressure as the pressure. The reflux turbulence intensity is set to the default value, and the wall function is used as the standard wall function.

3.3. Mathematical Model

Due to the constantly changing flow field and particle motion distribution over time, unsteady flow is used to simulate the movement of ratooning rice. Normally, the time step of the particle phase is less than or equal to that of the gas phase. The time step of the particle phase is related to the collision duration of the particle system, while the time step of the gas phase needs to consider whether the changes in boundary conditions and the motion of particles have a significant impact on the flow state. In the coupling process, to ensure the accuracy of particle motion simulation, the solid-phase time step is set to 1×10^{-6}, and the gas-phase time step is set to 1×10^{-4}. The air flowing inside the cleaning separation core is considered a viscous and compressible fluid. Considering the influence of the roughness of the cleaning separation core wall, the effect of surface tension is ignored [28]. Due to the large volume fraction of particles in the cleaning device, their impact on the flow field is significant, and their effect on the gas phase cannot be ignored. When using CFD-DEM coupling (EDEM 2018/Fluent17), the volume fraction term in the equation needs to be considered, so the Euler model is adopted. In the Euler model, the gas-phase continuity equation and momentum equation under two-phase flow are as follows [29]:

$$\frac{\partial(\varepsilon\rho)}{\partial t} + \nabla(\rho\varepsilon v) = 0 \tag{9}$$

$$\frac{\partial(\varepsilon\rho v)}{\partial t} + \nabla\left(\rho\varepsilon v^2\right) = -\nabla P + \nabla(\mu\varepsilon\nabla v) + \rho\varepsilon g - S \tag{10}$$

where ρ is the gas density, kg/m^3; v is the gas velocity, m/s; ε is the gas volume fraction phase; ∇ is a Hamiltonian differential operator; P is the pressure of gas microelements, Pa; g is the acceleration due to gravity, m/s^2; μ is the gas dynamic viscosity, Pa·s; and S is the momentum sink, N/m^3.

3.4. Particle Statistical Analysis

The airflow carries particles into the cleaning device, and the screening effect of the sieve intercepts the impurity particles with a particle size larger than the aperture and distributes them in various areas of the sieve. Considering the complex particle motion, wide distribution range, and randomness inside the spiral step cleaning device, this paper adopts a region division method to count the number of particles falling in different regions and uses the relative standard deviation *Sr* as a measurement index to assist in analyzing the uniformity of particle distribution on the screen surface [30]. *Sr* can reflect the particle distribution in different regions under different conditions:

$$S_r = \left[\frac{1}{(N-1)\overline{A}}\right]\sum_{i=1}^{N}(Z_i - \overline{A}) \tag{11}$$

where N is the number of blocks; Z_i is the number of particles in the area; and $\bar{A}$ is the average number of particles in the region. The smaller the *Sr*, the more uniform the particle distribution.

4. Simulation Result Analysis

4.1. Influence of Skeleton Thickness on Flow Field

Using a circular fluid calculation domain, the length of the calculation domain is 640 mm, and the diameter is 600 mm (the actual size of the cleaning chamber); the left end is set as the velocity inlet, and the right end is set as the pressure outlet. The value is one standard atmospheric pressure, and the cleaning separation core is located at the center of the calculation domain. Considering that excessively high airflow velocity can increase the loss rate and even block the impurity particle outlet of the cleaning separation core, the airflow inlet velocity is set to 14 m/s in the simulation. The gas flow field and streamline distribution in the cleaning separation core are shown in Figure 3. It can be observed that from the inlet to the outlet, the gas flow pressure rapidly increases while the gas flow velocity continuously decreases. The gas flow velocity at groove 6 is the lowest, at 11.72 m/s. The decrease in gas flow velocity at groove 6 is due to the semi-closed outlet of the cleaning separation core, but the gas flow velocity is still greater than 10 m/s, which can meet the basic conditions for particle movement.

When the thickness of the spiral-stepped skeleton is 20 mm, the maximum flow velocity inside the device is 18.6 m/s, and the maximum pressure is 340 pa. According to preliminary experiments, the suspension velocity range of ratooning rice grains is 7.8–13.1 m/s. The flow velocity can meet the requirements of ratooning rice cleaning. However, from the streamline diagram, it can be seen that most of the airflow directly passes through the sieve, without forming an effective vortex in the groove. The vortex size inside the groove is small, and weak vortices are extremely ineffective for separating rice grains and impurities and can even cause screen blockage problems. When the thickness of the spiral-stepped skeleton is 40 mm, the maximum flow velocity inside the device is 19.7 m/s, and the maximum pressure is 305 pa. From the streamline diagram, it can be seen that large vortices are formed in each cleaning groove. From the velocity cloud map, it can be seen that five-sixths of the area airflow velocity inside the cleaning device is high, and the airflow velocity in groove 6 is 16.3 m/s. The high airflow velocity ensures the cleaning effect. When the thickness of the spiral-stepped skeleton is 60 mm, the maximum flow velocity inside the device is 19.8 m/s, and the maximum pressure is 325 pa. Compared with the cleaning separation core with a skeleton thickness of 40 mm, the flow velocity changes slightly. However, from the streamline diagram, it can be seen that the vortex inside the groove gradually changes from circular to elliptical, the rotation trajectory of the mixture changes, and the outflow line of the device becomes more chaotic. The disorder of the airflow increases, and the disordered airflow is not conducive to the collection of ratooning rice grains. In addition, the thicker spiral skeleton occupies the effective space inside the device, which will reduce the efficiency of cleaning.

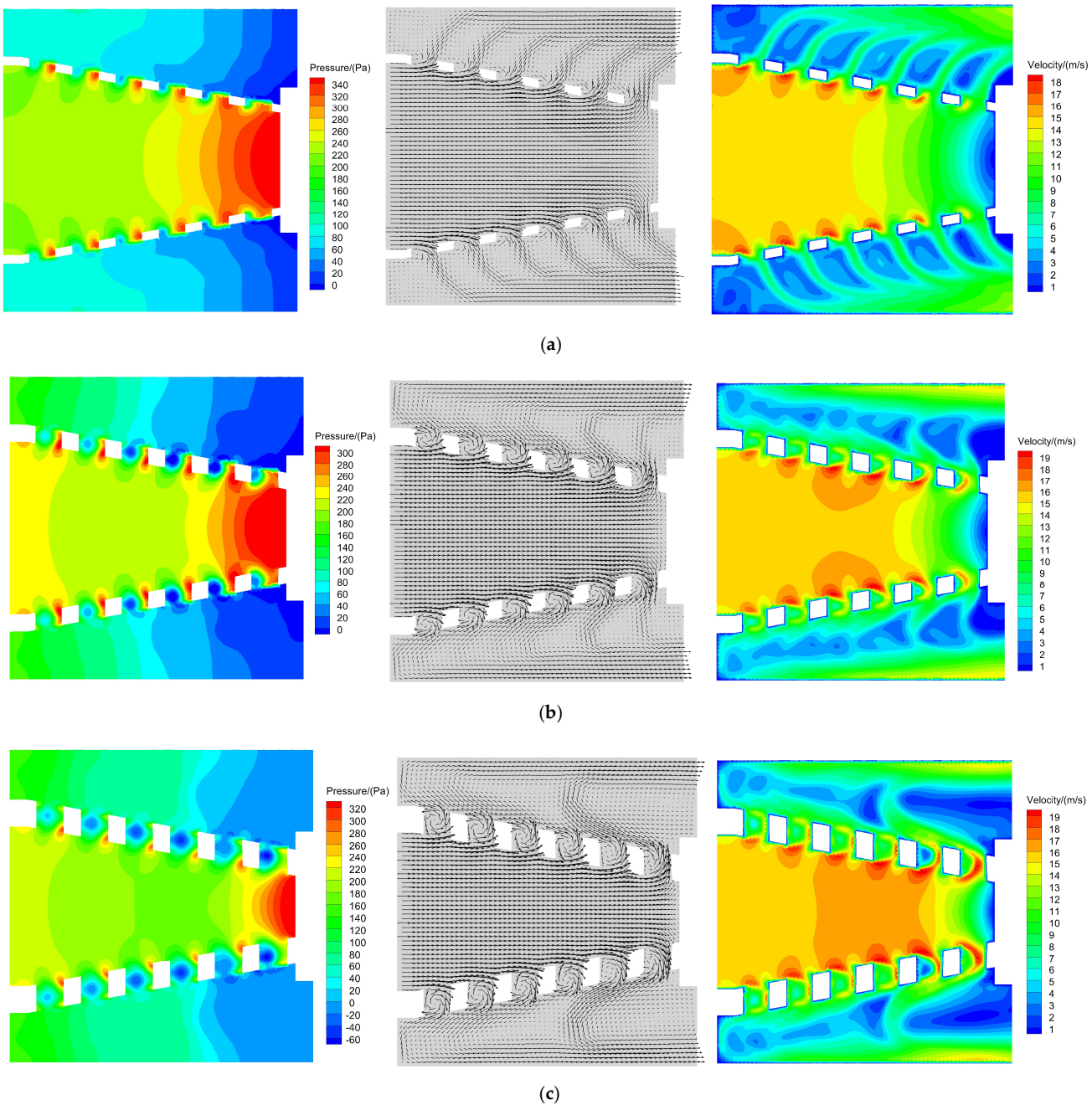

Figure 3. Velocity and pressure cloud maps of different spiral-stepped skeletons. (**a**) 20 mm. (**b**) 40 mm. (**c**) 60 mm.

4.2. Influence of Cone Angle on Flow Field

The gas flow field and streamline distribution inside the cleaning separation core under different cone angle conditions are shown in Figure 4. From the streamline diagram, it can be observed that as the cone angle increases, the average flow velocity inside the device increases, and the streamline gradually fluctuates. When the cone angle is 14.5°, the streamline fluctuation is most significant. The streamline near the cleaning groove is denser, and the dense curve represents the gathering of gas flow. The gathered gas flow will cause the mixture to agglomerate, and the agglomerated mixture will continuously deposit inside the spiral skeleton under the action of the gas flow, increasing the difficulty of cleaning. When the cone angle is 6.5°, the difference in area between the outlet and inlet of the device is not significant. The high-flow-velocity area is located near the first

three grooves. Due to the semi-closed design at the outlet, the area of the low-flow-velocity area near the centerline of the outlet is larger, while the area of the high-flow-velocity area in groove 6 is extremely small. The mixture located in the low-flow-velocity area will no longer move with the airflow after reaching the equilibrium state of force and will gradually accumulate, causing groove 6 to lose its cleaning ability. As the cone angle increases, the position of the high-velocity area moves toward the exit, and the area of low velocity near the outlet centerline decreases. The hindering effect of the low-velocity area on the cleaning performance of groove 6 continues to weaken. When the cone angle reaches 12.5°, the high-velocity area is located near grooves 2–5, and a crescent-shaped high-velocity area appears in groove 6. The area of low velocity near the outlet centerline is extremely small, and the lateral height of the low-velocity area is less than 20 mm. The small area of the low-velocity area in the device has little impact on the cleaning performance of groove 6. At this time, the spiral step cleaning device has an extremely excellent cleaning effect.

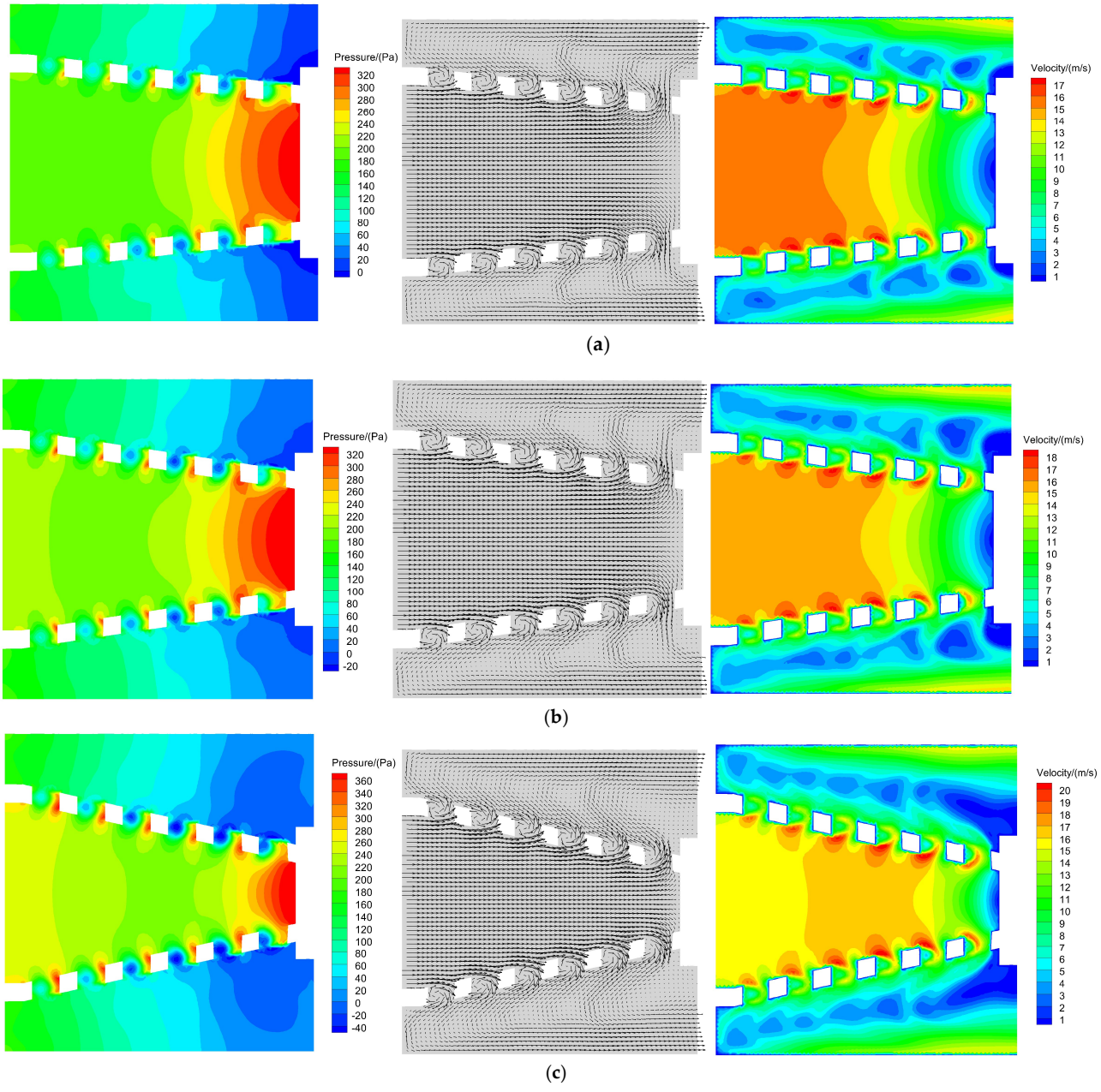

Figure 4. *Cont.*

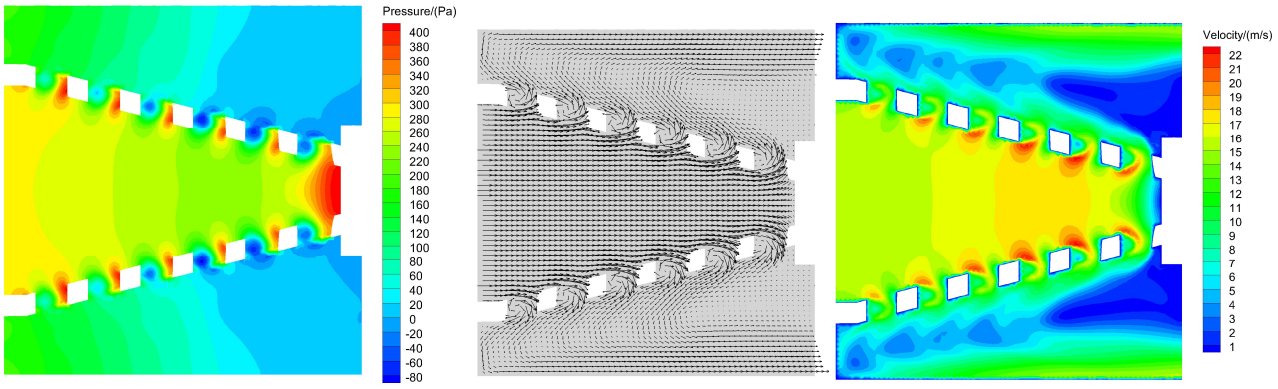

(**d**)

Figure 4. Influence of cone angle on flow field. (**a**) 6.5°. (**b**) 8.5°. (**c**) 12.5°. (**d**) 14.5°.

4.3. Analysis of Particle Movement Trajectory in the Groove

To facilitate the observation of particle motion in the groove, a local coupling simulation was conducted with a calculation domain length of 130 mm, as shown in Figure 5. Data processing is performed on the motion of particles in the groove at different time nodes within the target time period to obtain scatter plots of particle motion trajectories at multiple time nodes. These scatter plots of particle motion trajectories are then overlaid to obtain the stacked scatter plots of particle motion in grooves 1, 3, and 5 of the cleaning device under different inlet wind speeds. The sampling time period is 0.8~1.0 s, and the sampling interval is 0.01 s, as shown in Figure 6.

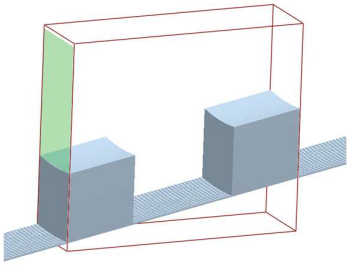

Figure 5. Computational domain.

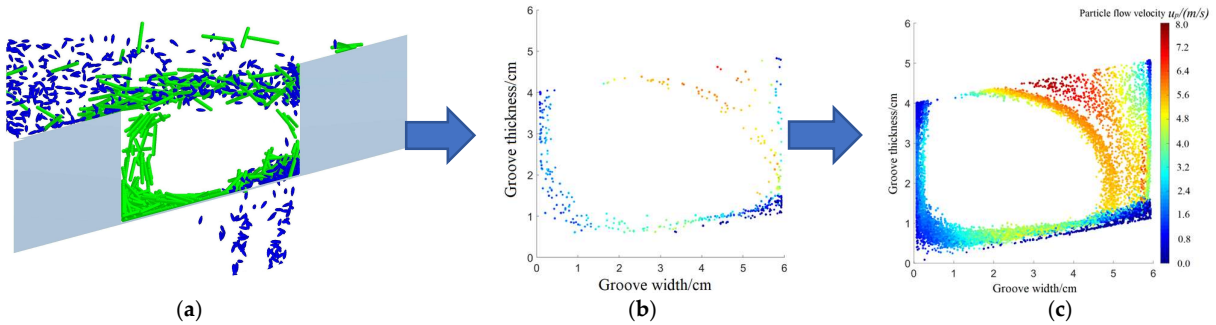

(**a**) (**b**) (**c**)

Figure 6. Process of motion trajectory analysis. (**a**) Particle movement in groove. (**b**) Scatter plot of motion trajectory (straw). (**c**) Overlay of scatter plot of motion trajectory (straw). Note: Blue particles, ratooning rice grains; green particles, straw.

From Figure 7, it can be seen that the mixture in the groove rapidly rotates clockwise under the action of the vortex, first colliding with the wall and then colliding with the sieve. Its motion trajectory is mainly distributed between the boundary of the vortex and the downstream skeleton. When the inlet velocity is low, there are two particle flows with

relatively concentrated motion trajectories in the groove, of which one follows the wall shear flow along the downstream skeleton, and the other moves along the vortex boundary. From the flow state analysis of each cleaning groove at the same flow velocity, it can be seen that the wall shear flow of the upstream skeleton is mainly laminar, with a lower average flow velocity and a smaller velocity gradient, while the wall shear flow of the downstream skeleton is mainly turbulent, with a higher flow velocity and a larger velocity gradient. The higher the velocity of the wall shear flow, the greater the velocity gradient, the faster the particles move, and the more pronounced the Brownian motion of the particles becomes. Therefore, the closer the cleaning groove is to the end of the cleaner, the more dispersed the trajectory of the wall particle flow becomes. Similarly, an increase in inlet velocity will also lead to an increase in wall shear flow velocity within the cleaning device, resulting in an increase in particle movement speed. According to the Stokes number, the followability of particles in a fluid is negatively correlated with their velocity. Therefore, the higher the inlet flow velocity, the closer the wrapped particle flow is to the downstream skeleton, and the larger the particle-free area in the groove becomes.

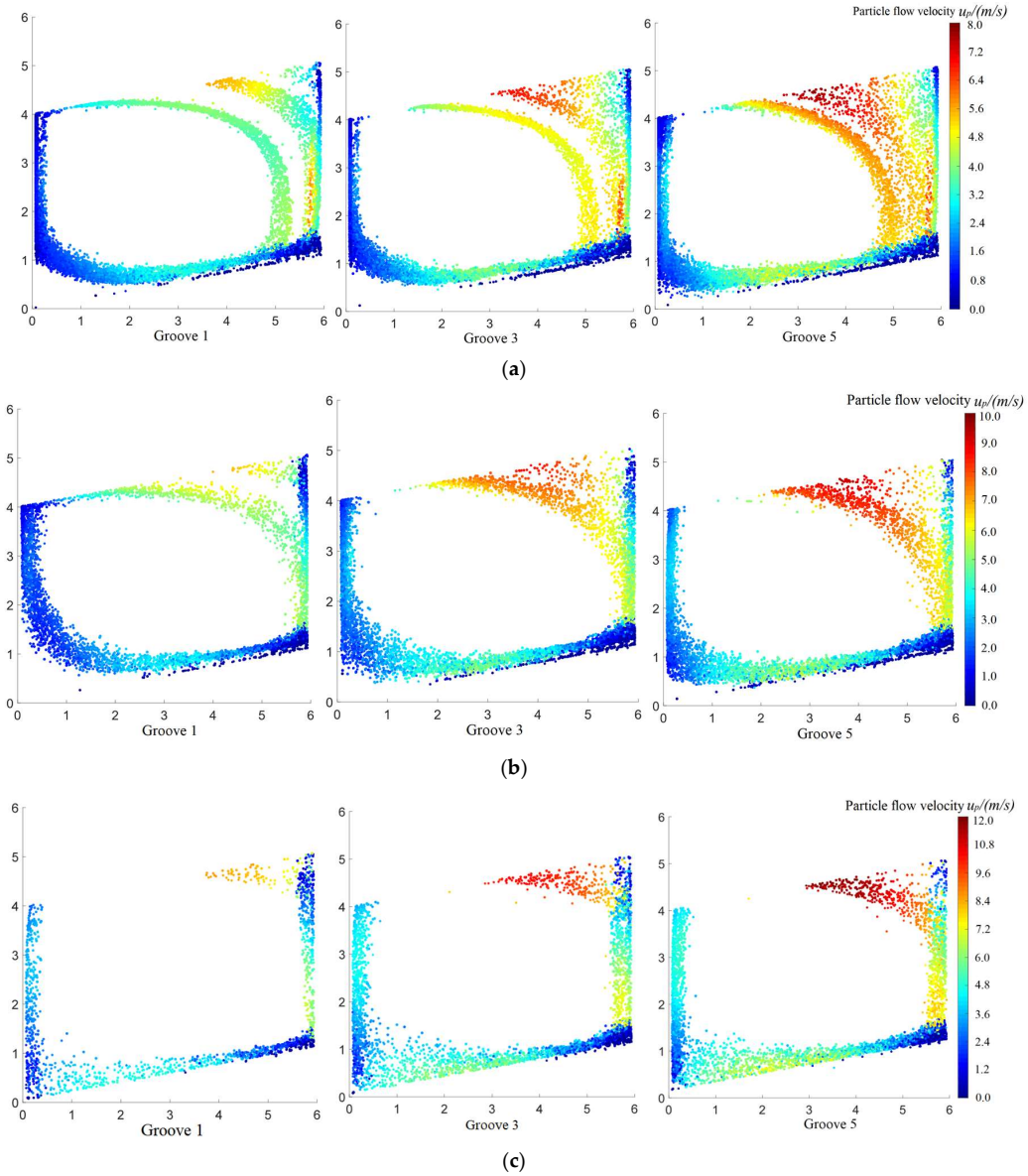

Figure 7. Particle motion trajectory scatter diagram. (**a**) Airflow velocity 8 m/s. (**b**) Airflow velocity 12 m/s. (**c**) Airflow velocity 16 m/s.

In addition, when the mixture reaches the front sieve, a portion of the ratooning rice particles will separate from the mesh surface, and the remaining particles will continue to return to the mainstream for the next rotational motion under the action of vortices. When the inlet flow velocity is 8 m/s, the velocity and drag force of the particles are relatively small, and gravity dominates. At this time, most of the particles on the front screen will be directly separated from the mesh surface. Therefore, the lower the inlet flow velocity, the more difficult it is for particles to enter the interior angle of the upstream skeleton groove. The rotational motion of particles can increase the risk of clogging in the middle screen, so from the perspective of anti-clogging, the step cleaning device should avoid working at too low an inlet flow velocity.

4.4. Particle Distribution in Groove

As shown in Table 3, upon comparing the total number of deposited impurity particles in the groove under different inlet flow velocities, it can be seen that with an increase in inlet flow velocity, the total number of impurity particles first increases, then decreases, and then increases again. When the inlet flow velocity is 8–11 m/s, as the inlet flow velocity increases, the amount of mixture entering the device increases, and the amount of impurities remaining in the device after cleaning also increases. When the inlet flow velocity is 12 m/s, the self-cleaning ability of the vortex gradually becomes apparent, and the total number of impurity particles in the groove shows a decreasing trend. When the inlet flow velocity is 13 m/s, the self-cleaning effect of the vortex reaches its optimum, and the total number of impurities in the groove reaches its lowest. At this time, the impurities are continuously and rapidly discharged from the device under the rotation and revolution of the vortex, and the cleaning efficiency reaches its optimum.

Table 3. Number of impurity particles in the groove at different inlet flow velocity.

Groove Number	Inlet Flow Velocity (m/s)								
	8	**9**	**10**	**11**	**12**	**13**	**14**	**15**	**16**
1	447	473	575	581	579	395	364	349	423
2	488 ※	499 ※	578	593	583	421	379	364	431
3	481	493	629 ※	638 ※	662 ※	447 ※	391	389	448
4	472	481	610	625	661	397	516 ※	416	435
5	468	467	589	618	620	405	461	553 ※	571 ※
6	488	512	648	659	585	424	435	605	585
Total	2844	2925	3629	3714	3690	1889	2546	2366	2893

Note: ※, peak value.

By comparing the particle quantity distribution in different cleaning grooves (excluding groove 6 at the outlet), it can be found that when the inlet flow velocity is less than 14 m/s, the impurity particles from groove 1 to groove 6 show a trend of first increasing and then decreasing, with peak values located in the first three grooves. When the inlet flow velocity is greater than 14 m/s, the peak number of impurity particles in the groove is located in groove 5. As the inlet flow velocity increases, the peak position of the number of impurity particles continues to move backward, from groove 2 to groove 5. When the peak position moves to groove 5, a large amount of particles accumulate, and the impurity outlet near groove 6 cannot discharge the impurity particles in a timely manner. The number of particles in the device increases, and the cleaning efficiency decreases.

The number of impurity particles in the groove is mainly affected by the cleaning flow velocity and shear flow velocity in the groove. The cleaning flow velocity direction is perpendicular to the screen mesh, while the shear flow velocity direction is parallel to the screen mesh surface. When the inlet flow velocity is low, there are fewer particles entering the groove, and the cleaning flow velocity of the cleaning groove is also low. Gravity plays a major role, and particles are not easily deposited in the interior of the groove. At this time, the cleaning flow velocity in the groove is the main factor affecting the number of

impurity particles in the groove. As the inlet flow velocity increases, the overall cleaning flow velocity increases, and the number of particles entering the groove also increases. The increase in shear flow velocity not only causes the deposition of impurity particles in the two inner corners of the groove but also reduces the deposition of particles on the middle screen. At this time, the shear flow velocity in the groove becomes the main factor affecting the number of impurity particles.

When the inlet velocity increases from 8 m/s to 11 m/s, the enhancement of shear flow leads to a continuous increase in impurity particles on the mesh surface, and the peak number of impurity particles in the groove gradually shifts from groove 2 to groove 3. When the inlet flow velocity exceeds 12 m/s, the shear flow on the mesh surface in each cleaning groove reaches a high level, and the number of impurity particles on the mesh surface is significantly reduced.

5. Bench Test

5.1. Experimental Scheme

In order to verify the feasibility of CFD-DEM coupling, a cleaning performance test was conducted indoors at the College of Agricultural Engineering, Jiangsu University, on 25 August 2024. The experimental ratooning rice was Longliang Youhua, and the moisture content of ratooning rice during the experiment was 31.5%. As shown in Figure 8, the experimental device consists of a fan (Hon&Guan HP-315PE, Zhenjiang, China), a mixing chamber, a cleaning chamber, and a support platform. The cleaning chamber is equipped with a cleaning separation core and a sieve. The grain mixture passes through the feeding trough and cleaning chamber in sequence under the action of the fan. The airflow speed can be infinitely adjusted through a frequency converter, with a wind speed range of 0–20 m/s. The impurity collection box and the clean grain collection box are both located below the cleaning room. The measurement of wind speed uses the Ecovacs AS-H5 high-precision anemometer (Measurement range 0–50 m/s).

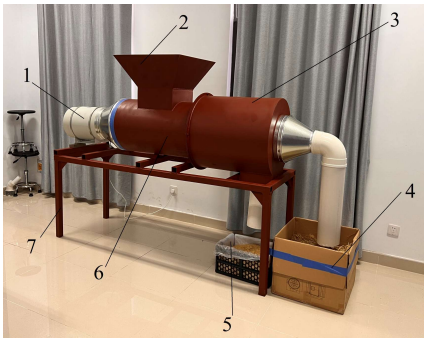

Figure 8. Structure diagram of spiral step cleaning device. (1) Fan, (2) feeding trough, (3) cleaning chamber, (4) impurity collection box, (5) clean grain collection box, (6) mixing chamber, (7) support table.

During the experiment, the mixture material was manually fed, with a total feeding mass of 30 kg. After the experiment, the number of impurity particles in the clean grain collection box was counted, and the grain impurity rate was calculated. The number of ratooning rice grains in the impurity collection box was counted, and the grain loss rate was calculated. The blockages on the separation core were weighed, and the blockage rate was calculated. Each experiment was repeated three times to calculate the grain impurity rate, grain loss rate, and sieve clogging rate. The calculation method is as follows:

$$\begin{cases} Y_1 = \frac{m_k}{m_k + m_i} \times 100\% \\ Y_2 = \frac{m_l}{m_r} \times 100\% \\ Y_3 = \frac{m_c}{m_h + m_r} \times 100\% \end{cases} \quad (12)$$

where Y_1, Y_2, and Y_3 are the grain impurity rate, grain loss rate, and sieve clogging rate, respectively, %; m_k is the mass of impurities in the clean grain collection box, g; m_i is the mass of ratooning rice grains in the clean grain collection box, g; m_l is the mass of ratooning rice grains in the impurity collection box, g; m_r is the total mass of ratooning rice grains fed, g; m_c is the mass of blockages on the cleaning separation core, g; and m_h is the total mass of impurities fed in, g.

5.2. Bench Optimization Test

5.2.1. Experimental Methods and Design

In order to obtain the optimal operating parameters of the spiral step cleaning device, wind speed, feeding rate, and device inclination angle were selected as experimental factors. A three-factor quadratic regression orthogonal rotation combination experiment was conducted, with grain impurity rate, grain loss rate, and sieve clogging rate as evaluation indicators. Each experiment was repeated three times, and the average value was taken. The experimental factor codes and results are shown in Tables 4 and 5, where X_1, X_2, and X_3 represent the fan speed, feeding rate, and device inclination angle, respectively. Y_1, Y_2, and Y_3 represent the grain impurity rate, grain loss rate, and sieve clogging rate, respectively.

Table 4. Experimental factors of codes.

Code	Fan Speed X_1/(r·min^{-1})	Feed Rate X_2/(kg/s)	Device Inclination Angle X_3/(°)
−1.682	2500	2.5	0
−1	2601	2.91	1.01
0	2750	3.5	2.5
1	2898	4.09	2.29
1.682	3000	4.5	5

Table 5. Experiment design and results.

No.	Factor			Result		
	Drum Speed X_1/(r·min^{-1})	Flexible Body Thickness X_2/(mm)	Rod Tooth Length X_3/(mm)	Y_1/%	Y_2/%	Y_3/%
1	−1	−1	−1	2.22	1.81	3.33
2	1	−1	−1	1.94	1.61	3.67
3	−1	1	−1	2.03	2.82	4.21
4	1	1	−1	1.76	1.43	3.54
5	−1	−1	1	2.24	2.55	3.31
6	1	−1	1	1.33	2.32	2.96
7	−1	1	1	1.26	1.44	3.67
8	1	1	1	2.64	2.45	4.03
9	−1.682	0	0	1.95	1.74	3.65
10	1.682	0	0	2.14	1.32	4.63
11	0	−1.682	0	2.42	2.88	3.66
12	0	1.682	0	1.56	2.53	4.08
13	0	0	−1.682	1.68	2.35	3.66
14	0	0	1.682	2.11	1.43	2.85
15	0	0	0	2.05	1.57	2.72
16	0	0	0	1.68	2.84	3.14
17	0	0	0	1.46	1.04	2.93
18	0	0	0	1.32	2.08	2.45
19	0	0	0	2.53	1.56	1.99
20	0	0	0	2.85	2.05	2.84
21	0	0	0	2.01	1.45	3.01
22	0	0	0	1.53	2.53	3.78
23	0	0	0	1.74	2.14	4.43

5.2.2. Establishment and Significance Testing of Regression Mathematical Models

Multiple regression fitting was performed on the experimental data using Design Expert 8.0.6 software, and regression analysis was performed on the experimental results to obtain regression equations for grain impurity rate Y_1, grain loss rate Y_2, and sieve clogging rate Y_3, respectively:

$$Y_1 = -13.004 + 0.011X_1 + 0.205X_2 + 0.022X_3 + 0.00002828X_1X_2 + 0.00002627X_1X_3 - 0.0084X_2X_3 - 0.0000019X_1^2 - 0.042X_2^2 - 0.013X_3^2 \quad (13)$$

$$Y_2 = 147.41 - 0.115X_1 + 3.644X_2 + 1.074X_3 - 0.00221.23X_1X_2 - 0.00071X_1X_3 + 0.035X_2X_3 + 0.000023X_1^2 + 0.226X_2^2 + 0.236X_3^2 \quad (14)$$

$$Y_3 = 330.94 - 0.202X_1 - 17.66X_2 - 3.54X_3 + 0.004X_1X_2 + 0.00057X_1X_3 + 0.37X_2X_3 + 0.000032X_1^2 + 1.12X_2^2 + 0.053X_3^2 \quad (15)$$

The significance test of the regression equation is shown in Table 6. According to Table 6, the fitting degree of the model is extremely significant ($p < 0.01$). However, the P-values of the interaction terms are all greater than 0.1, indicating that the above factors have no significant impact on the experimental indicators. All other tests are significant, indicating that the influence of relevant experimental factors on the response values is not a simple linear relationship but a quadratic relationship. The regression model after removing insignificant factors is as follows:

$$Y_1 = -13.36 + 0.011X_1 + 0.262X_2 + 0.054X_3 - 0.0000019X_1^2 - 0.042X_2^2 - 0.013X_3^2 \quad (16)$$

$$Y_2 = 173.06 - 0.124X_1 - 2.296X_2 - 0.746X_3 + 0.000023X_1^2 + 0.226X_2^2 + 0.236X_3^2 \quad (17)$$

$$Y_3 = 285.721 - 0.187X_1 - 5.85X_2 - 0.7X_3 + 0.000032X_1^2 + 1.23X_2^2 + 0.053X_3^2 \quad (18)$$

Table 6. Variance analysis of regression equation.

Variance Source	Grain Impurity Rate				Grain Loss Rate				Sieve Clogging Rate			
	Square Sum	Freedom Degree	F	P	Square Sum	Freedom Degree	F	P	Square Sum	Freedom Degree	F	P
Model	0.065	9	23.23	<0.0001 **	20.79	9	7.9	0.0005 **	106	9	23.37	<0.0001 **
X_1	0.007541	1	24.37	0.0003 **	3.62	1	12.36	0.0038 **	50.59	1	100.39	<0.0001 **
X_2	0.006081	1	19.65	0.0007 **	2.45	1	8.36	0.0126 *	36.80	1	73.02	<0.0001 **
X_3	0.004028	1	13.02	0.0032 **	5.69	1	19.46	0.0007 **	5.74	1	11.39	0.0050 **
X_1X_2	0.00005	1	0.16	0.6943	0.30	1	1.03	0.3294	0.98	1	1.94	0.1866
X_1X_3	0.0002	1	0.65	0.4359	0.20	1	0.67	0.4286	0.12	1	0.25	0.6268
X_2X_3	0.00045	1	1.45	0.2494	0.007813	1	0.027	0.8727	0.84	1	1.68	0.2179
X_1^2	0.0030	1	96.24	<0.0001 **	4.18	1	14.3	0.0023 **	7.79	1	15.45	0.0017 **
X_2^2	0.00358	1	11.57	0.0047 **	0.10	1	0.35	0.5655	3.01	1	5.96	0.0297 *
X_3^2	0.0014	1	43.63	<0.0001 **	4.33	1	14.80	0.0020 **	0.22	1	0.43	0.5237
Residual	0.004023	13			3.80	13			6.55	13		
Lack of fit	0.002223	5	1.98	0.1869	2.64	5	3.62	0.0523	4.45	5	3.39	0.0612
Error	0.0018	8			1.17	8			2.10	8		
Sum	0.069	22			24.60	22			112.55	22		

Note: * significant ($p < 0.05$) and ** extremely significant ($p < 0.01$).

5.2.3. Response Surface Analysis

(1) Interaction of Fan Speed and Feeding Rate

Figure 9a shows the response surface of the interaction between fan speed and feeding rate on the grain impurity rate when the device inclination angle is 2.5°. As shown in the figure, the grain impurity rate increases with the increase in feeding rate, and the relationship between grain impurity rate and feeding rate is a quadratic curve. It can be inferred that when the feeding rate is too large, the device cannot handle the excess mixture in a timely manner, resulting in an increase in the impurity content of the grains. The

grain impurity rate first decreases and then increases with the increase in fan speed. When the fan speed is 2782 r/min, the grain impurity rate reaches its lowest value at different feeding rates.

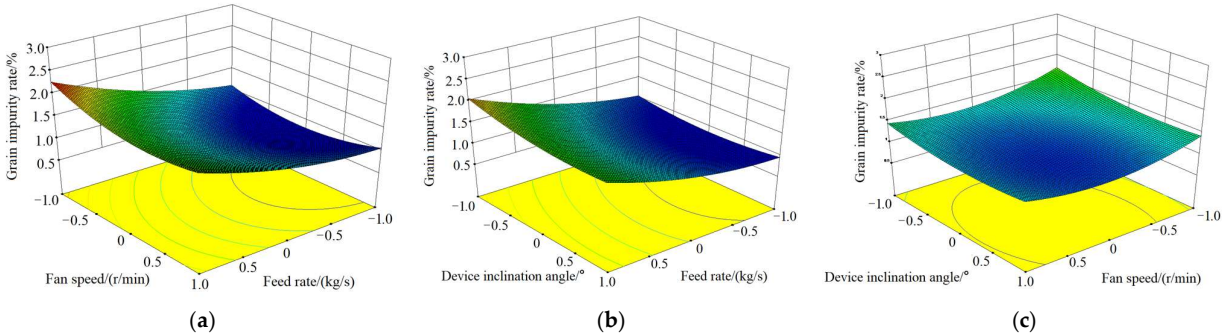

(**a**) (**b**) (**c**)

Figure 9. Effects of interactive factors on the grain impurity rate. (**a**) The influence of fan speed and feed rate on grain impurity rate. (**b**) The influence of device inclination angle and feed rate on grain impurity rate. (**c**) The influence of device inclination angle and fan speed on grain impurity rate.

(2) Interaction between feeding rate and device inclination angle

Figure 9b shows the response surface diagram of the interaction between feeding rate and device inclination angle on grain impurity rate when the fan speed is 2750 r/min. As shown in the figure, the relationship between grain impurity rate and feeding rate follows a quadratic curve. As the feeding rate increases, the grain impurity rate increases rapidly. The relationship between the grain impurity rate and device inclination angle is a quadratic curve. When the device inclination angle is 0–2.5°, the grain impurity rate decreases with an increase in device inclination angle. When the device inclination angle is 2.5–5°, the grain impurity rate increases with an increase in device inclination angle.

(3) Interaction between fan speed and device inclination angle

Figure 9c shows the response surface of the interaction between fan speed and device inclination angle on the grain impurity rate when the feeding rate is 3.5 kg/s. As shown in the figure, when the fan speed is constant, as the inclination angle of the device increases, the grain impurity rate first decreases and then increases. When the inclination angle of the device is constant, as the fan speed increases, the grain impurity rate first decreases and then increases.

5.2.4. Optimal Parameters

The grain impurity rate, grain loss rate, and screen clogging rate are minimized, and the parameters are optimized as follows: when the device inclination angle is 2.47°, the fan speed is 2906 r/min, and the feeding rate is 4.0 kg/s, the grain impurity rate, grain loss rate, and screen clogging rate are 2.21%, 2.15%, and 3.5%, respectively. When the fan speed is 2900 r/min, the wind speed is 14.17 m/s.

The results of the bench test are consistent with the simulation results. Excessive wind speed will cause the peak position of particles to move toward the outlet, thereby blocking the sieve and affecting the cleaning effect of the spiral step cleaning device. This proves that using CFD-DEM to simulate the cleaning process of ratooning rice is feasible. The reason for the difference between the two is that in the simulation, the mixture only consists of straw and ratooning rice grains, while in the actual experiment, there are impurities such as leaves in the mixture. In addition, the assembly gap between different components in the bench test is also the reason for the difference in the results between the two. The above reasons make the simulation results slightly better than the bench test results.

The optimization results were experimentally verified and compared with traditional cleaning systems, as shown in Table 7. Under the optimal parameters, the actual values were close to the simulated analysis values, and the grain impurity rate, grain loss rate,

and screen clogging rate were all better than the traditional cleaning system, with values reduced by 44.5%, 39.6%, and 83.9%, respectively.

Table 7. Comparative analysis of results.

Item	Simulation Result	Bench Test		
		Spiral Step Cleaning Device	Traditional Cleaning Device	Optimization Rate/%
Grain impurity rate/%	2.06	2.21	3.98	44.5
Grain loss rate/%	1.96	2.15	3.56	39.6
Sieve clogging rate/%	3.14	3.50	21.7	83.9

6. Conclusions

This paper uses the CFD-DEM coupling method to analyze the internal flow field of the cleaning separation core and the movement of particles. The influence of the cone angle and spiral skeleton thickness on the cleaning effect was studied, and the conclusions are as follows:

(1) Aiming at the problem that traditional cleaning devices are not suitable for cleaning ratooning rice, a spiral step cleaning device was designed by integrating mechanical and pneumatic combination separation technology, and the structural parameter range of the cleaning device was determined.

(2) The influence of spiral skeleton thickness and cone angle on the airflow field was analyzed by using the CFD-DEM coupling method. The results indicate that as the thickness of the spiral skeleton increases, the peak flow velocity continuously increases, the vortex gradually changes from circular to elliptical, the disorder of the airflow increases, and the entrainment effect on particles weakens. As the cone angle increases, the position of the high-velocity area moves toward the exit, and the area of the low velocity near the outlet centerline decreases. The hindering effect of the low-velocity area on the cleaning performance of groove 6 continues to weaken. When the cone angle is 12.5°, the high-velocity area is located from grooves 2 to 5, and the area of low velocity near the outlet centerline is extremely small, which has an excellent cleaning effect.

(3) The range of wind speed values was determined by overlaying scatter plots of particle motion trajectories, and the distribution of impurity particles in the groove under different inlet flow velocities was statistically analyzed. It was found that as the inlet flow velocity increased, the total number of impurity particles first increased, then decreased, and then increased again. The peak position of impurity particle quantity gradually shifts backward. When the inlet flow velocity is below 13 m/s, there are too many impurity particles in the groove. When the inlet flow velocity is greater than 14 m/s, the sieve is prone to clogging.

(4) A three-factor quadratic regression orthogonal rotation combination experiment was conducted with fan speed, feeding rate, and device inclination angle as experimental factors. The results showed that when the device inclination angle was 2.47°, fan speed was 2906 r/min, and feeding rate was 4.0 kg/s, the grain impurity rate, grain loss rate, and screen clogging rate were 2.21%, 2.15%, and 3.5%, respectively. Compared with traditional cleaning systems, these values were reduced by 44.5%, 39.6%, and 83.9%, respectively. The results of the bench test were consistent with the simulation results, indicating that using the CFD-DEM coupling method to optimize the structural parameters of the device is feasible.

Author Contributions: Conceptualization, Z.W.; data curation, W.L.; funding acquisition, Z.W.; investigation, W.L.; methodology, W.L.; project administration, Z.W.; software, S.Z.; validation, W.L. and S.Z.; writing—original draft, W.L.; writing—review & editing, S.Z. All authors have read and agreed to the published version of the manuscript.

Funding: This research was funded by the Key Core Technology Research Project of the Ministry of Agriculture and Rural Affairs on Agricultural Production: Light and Simple Grain Combine Harvester (NK2022160401) and Jiangsu Funding Program for Excellent Postdoctoral Talent.

Institutional Review Board Statement: Not applicable.

Informed Consent Statement: Not applicable.

Data Availability Statement: The data that support the findings of this study are available on request from the corresponding author.

Acknowledgments: The authors gratefully acknowledge the editors and anonymous reviewers for their constructive comments on our manuscript.

Conflicts of Interest: The authors declare no conflicts of interest.

References

1. Zhao, Z.; Huang, H.; Yin, J.; Yang, S. Dynamic analysis and reliability design of round baler feeding device for rice straw harvest. *Biosyst. Eng.* **2018**, *174*, 10–19. [CrossRef]
2. Xing, S.; Yu, Y.; Cao, G.; Hu, J.; Zhu, L.; Liu, J.; Wu, Q.; Li, Q.; Xu, L. Design and Parametric Optimization Study of an Eccentric Parallelogram-Type Uprighting Device for Ratoon Rice Stubbles. *Agriculture* **2024**, *14*, 534. [CrossRef]
3. Liu, W.; Zeng, S.; Chen, X. Design and experiment of spiral step cleaning device for ratooning rice based on CFD-DEM coupling. *Comput. Electron. Agric.* **2024**, *224*, 109207. [CrossRef]
4. Yang, T.; Zhang, H.; Li, F.; Yang, T. Optimized Tillage Method Increased Rice Yield in Rice Ratooning System. *Agriculture* **2024**, *14*, 1768. [CrossRef]
5. Liu, W.; Luo, X.; Zeng, S. The Design and Test of the Chassis of a Triangular Crawler-Type Ratooning Rice Harvester. *Agriculture* **2022**, *12*, 890. [CrossRef]
6. Liu, W.; Luo, X.; Zeng, S. Performance test and analysis of the self-adaptive profiling header for ratooning rice based on fuzzy PID control. *Trans. Chin. Soc. Agric. Eng.* **2022**, *38*, 1–9.
7. Liu, W.; Zeng, S.; Chen, X. Design and Experiment of Adaptive Profiling Header Based on MultiBody Dynamics–Discrete Element Method Coupling. *Agriculture* **2024**, *14*, 105. [CrossRef]
8. Lin, J.; Gu, M.; Luo, W.; Shen, H.; Hu, Z.; Gu, F.; Wu, F.; Zhang, P.; Xu, H. Simulation Analysis and Test of a Cleaning Device for a Fresh-Peanut-Picking Combine Harvester Based on Computational Fluid Dynamics–Discrete Element Method Coupling. *Agriculture* **2024**, *14*, 1594. [CrossRef]
9. Wu, T.; Li, F.; Liu, Q.; Ren, J.; Huang, J. Numerical Simulation and Analysis of the Impurity Removal Process of a Sugarcane Chopper Harvester Based on a CFD–DEM Model. *Agriculture* **2024**, *14*, 1392. [CrossRef]
10. Fang, W.; Wang, X.; Zhu, C.; Han, D.; Zang, N. Analysis of Film Unloading Mechanism and Parameter Optimization of Air Suction-Type Cotton Plough Residual Film Recovery Machine Based on CFD-DEM Coupling. *Agriculture* **2024**, *14*, 1021. [CrossRef]
11. Zhang, H.; Pan, F.; Han, D. Design and Test of a Crawler-Type On-Film Precision Cotton Seeding Device on DEM-CFD. *Agriculture* **2024**, *14*, 962. [CrossRef]
12. Sanderson, S.L.; Roberts, E.; Lineburg, J.; Brooks, H. Fish mouths as engineering structures for vortical cross-step filtration. *Nat. Commun.* **2016**, *7*, 11092. [CrossRef] [PubMed]
13. Qian, D.; Cheng, Q.; Li, G.; Zhao, Y. Experimental research on reducing power consumption of pneumatic conveying of wheat. *Trans. Chin. Soc. Agric. Eng.* **2003**, *19*, 108–111.
14. Wei, H.; Xie, H.; Hu, Z.; Yan, J.; Liu, M.; Xu, H. Parameter optimization and test of pneumatic conveying equipment for peanut pods. *Trans. Chin. Soc. Agric. Eng.* **2016**, *32*, 6–12.
15. Mamtimin, G.; Jahep, A.; Orkin, R.; Gulbahar, T.; Jin, A. Theoretical algorithm and experimental verification of seed cotton ball suspension velocity. *Trans. Chin. Soc. Agric. Eng.* **2022**, *38*, 52–62.
16. Liu, W.; Luo, X.; Zeng, S.; Wen, Z. Numerical simulation and experiment of grain motion in the conveying system of ratooning rice harvesting machine. *Int. J. Agric. Biol. Eng.* **2022**, *15*, 103–115. [CrossRef]
17. Akhshik, S.; Behzad, M.; Rajabi, M. CFD-DEM approach to investigate the effect of drill pipe rotation on cuttings transport behavior. *J. Pet. Sci. Eng.* **2015**, *127*, 229–244. [CrossRef]
18. Qiao, M.; Xia, G.; Cui, T.; Xu, Y.; Gao, X. Effect of moisture, protein, starch, soluble sugar contents and microstructure on mechanical properties of maize kernels. *Food Chem.* **2022**, *379*, 132147. [CrossRef]
19. Su, Y.; Cui, T.; Xu, Y.; Gao, X. A combined experimental and DEM approach to optimize the centrifugal maize breakage tester. *Powder Technol.* **2022**, *397*, 117008. [CrossRef]
20. Dai, F.; Song, X.; Zhao, W.; Han, Z.; Zhang, F.; Zhang, S. Motion simulation and test on threshed grains in tapered threshing and transmission device for plot wheat breeding based on CFD-DEM. *Int. J. Agric. Biol. Eng.* **2019**, *12*, 66–73. [CrossRef]
21. Li, H.; Li, Y.; Gao, F.; Zhao, Z.; Xu, L. CFD-DEM simulation of material motion in air-and-screen cleaning device. *Comput. Electron. Agric.* **2012**, *88*, 111–119. [CrossRef]

22. Stel, H.; Franco, A.T.; Junqueira, S.L.M.; Erthal, R.H.; Mendes, R.; Gonçalves, M.A.L.; Morales, R.E.M. Turbulent flow in d-type corrugated pipes: Flow pattern and friction factor. *J. Fluids Eng.* **2012**, *134*, 121202. [CrossRef]
23. Brooks, H.; Haines, G.E.; Lin, M.C. Physical modeling of vortical cross-step flow in the American paddlefish. Polyodon Spathula. *PLoS ONE* **2018**, *13*, e0193874. [CrossRef]
24. Liu, C.; Chung, T. Forced convective heat transfer over ribs at various separation. *Int. J. Heat Mass Tran.* **2012**, *55*, 5111–5119. [CrossRef]
25. Schroeder, A.; Marshall, L.; Trease, B.; Becker, A.; Sanderson, S. Development of helical, fish-inspired cross-step filter for collecting harmful algae. *Bioinspir. Biomim.* **2019**, *14*, 056008. [CrossRef]
26. Smith, J.; Sanderson, S. Particle retention in suspension-feeding fish after removal of filtration structures. *Zoology* **2013**, *116*, 348–355. [CrossRef]
27. Zhao, Z.; Li, Y.; Liang, Z.; Gong, Z. DEM simulation and physical testing of rice seed impact against a grain loss sensor. *Biosyst. Eng.* **2013**, *116*, 410–419.
28. Gao, X.; Cui, T.; Zhou, Z. DEM study of particle motion in a novel high-speed seed metering device. *Adv. Powder Technol.* **2021**, *32*, 1438–1449. [CrossRef]
29. Yuan, J.; Wu, C.; Li, H.; Qi, X.; Xiao, X.; Shi, X. Movement rules and screening characteristics of rice-threshed mixture separation through a cylinder sieve. *Comput. Electron. Agric.* **2018**, *154*, 320–329. [CrossRef]
30. Zhou, L.; Han, D.; Yu, L.; Li, N.; Guo, H.; Wang, Z. Effects of guide vanes on performance of Y-screen filter. *Trans. Chin. Soc. Agric. Eng.* **2020**, *36*, 40–46.